AIMS *Mathematics*

Research article

Fuzzy adaptive learning control network (FALCN) for image clustering and content-based image retrieval on noisy dataset

S. Neelakandan[1], Sathishkumar Veerappampalayam Easwaramoorthy[2], A. Chinnasamy[3] and Jaehyuk Cho[2,*]

[1] Department of CSE, R.M.K. Engineering College, Chennai, 601206, India
[2] Department of Software Engineering, Jeonbuk National University, Jeonju-si, Jeollabuk-do, 54896, Republic of Korea
[3] Department of Data Science and Business Systems, School of Computing, SRMIST Kattankulathur, Chennai, 603023, India

* Correspondence: Email: chojh@jbnu.ac.kr.

Abstract: It has been demonstrated that fuzzy systems are beneficial for classification and regression. However, they have been mainly utilized in controlled settings. An image clustering technique essential for content-based picture retrieval in big image datasets is developed using the contents of color, texture and shape. Currently, it is challenging to label a huge number of photos. The issue of unlabeled data has been addressed. Unsupervised learning is used. K-means is the most often used unsupervised learning algorithm. In comparison to fuzzy c-means clustering, K-means clustering has lower-dimensional space resilience and initialization resistance. The dominating triple HSV space was shown to be a perceptual color space made of three modules, S (saturation), H (hue) and V (value), referring to color qualities that are significantly connected to how human eyes perceive colors. A deep learning technique for segmentation (RBNN) is built on the Gaussian function, fuzzy adaptive learning control network (FALCN), clustering and the radial basis neural network. The segmented image and critical information are fed into a radial basis neural network classifier. The suggested fuzzy adaptive learning control network (FALCN) fuzzy system, also known as the unsupervised fuzzy neural network, is very good at clustering images and can extract image properties. When a conventional fuzzy network system receives a noisy input, the number of output neurons grows needlessly. Finally, random convolutional weights extract features from data without labels. Furthermore, the state-of-the-art uniting the proposed FALCN with the RBNN classifier, the proposed descriptor also achieves comparable performance, such as improved accuracy is 96.547 and reduced mean squared error of 36.028 values for the JAFE,

ORL, and UMIT datasets.

1. Introduction

The use of multimedia strategies has facilitated access to photographs with additional information. Utilizing low-level image attributes, content-based image retrieval (CBIR) searches a sizable database for the requested pictures. The following are examples of low-level picture attributes: color, edge quality and orientation [1]. CBIR is used by digital libraries [2], e-commerce [3] and medical imaging [4]. Examples of image retrieval methods include text-based image retrieval and sketch-based image retrieval, to name only two. The image search on Text-Based Image Retrieval (TBIR) makes use of labels and keywords. The most efficient application is Google Images. Consequently, verbal descriptions may include unrelated information. Large databases make manual annotation complex [5].

An image recovery system recovers images using user-created sketches [6]. The Soft Histogram of Edge Local Orientation, which enhances sketch-based picture retrieval, uses local orientation [7]. However, this issue is resolved by the suggested histogram of line relationships (HLR). It determines the best edge form to match object limits and removes noisy edges [8]. It provides an analog relevance feedback mechanism for retrieval optimization depending on user intent [9]. In order to improve retrieval performance, case-based long-term learning (CB-LTL) [10] takes into account the user's goals while providing pertinent feedback. [11] Mandal and his colleagues created the S-BoVW, a signature-based bag of visual words. Scrambled words match an image's texture and color using this retrieval technique. BoVW-based approaches boost retrieval performance, but they cost a lot to compute.

Traditional methods for indexing pictures in image files need to be changed, be made easier and take less time. The primary input that CBIR requires is a query image, and it compares the query image's visual data to the images in the archive. It also searches for characteristics in closely related photos. When a photo or sketch is put into the system, it looks for other pictures that look like it. This method gets rid of the need to describe an image's visual information in words while staying close to how people see visual data [12].

Fuzzy systems make decisions by fuzzifying sharp inputs, putting fuzzy outputs to use and using fuzzy logic. Fuzzy logic is a powerful technique for managing uncertainty in raw data compared to other computational intelligence techniques [13]. Fuzzy approaches are widely employed in conjunction with fusion strategies to efficiently merge data from many sources, producing more meaningful data representation [14].

More storage space is required than ever due to the exponential growth of digital image applications. Because it is significantly less expensive than hardware upgrades and infrastructure reorganization, cloud storage is a popular alternative for processing large amounts of data. Image-based data is becoming significant in various presentations and disease diagnoses, including face identification and object recognition [15]. Cloud computing decreases the need for local hardware stores and enables image processing programmed to leverage cloud computing power by uploading large photo databases to the cloud server. Since photos generally contain sensitive and personal

information, cloud-based outsourcing of image datasets creates privacy problems.

Fuzzy clustering-based picture segmentation is a popular field of study in image processing and computer vision. However, several gaps in the existing literature still require further research. Some of the research gaps in fuzzy clustering-based image segmentation are robustness to noise (Most fuzzy clustering-based image segmentation techniques are sensitive to noise in the image. Developing robust strategies for noise is still an active area of research.) and evaluation metrics (More standard evaluation metrics must be used to compare different fuzzy clustering-based image segmentation techniques. Developing traditional evaluation metrics that can objectively evaluate the performance of these techniques is an open research problem [16]).

The primary driving force behind this research is the possibility that Gaussian function fuzzy adaptive learning control network (FALCN) and radial basis neural network (RBNN) could find significant practical applications in fields like computer vision, image processing and machine learning, where precise image clustering and retrieval are crucial. The authors may have attempted to enhance the precision and efficiency of picture grouping and retrieval tasks by creating a more robust method to handle noise in image datasets [17]. The use of a fuzzy adaptive learning control network may be a novel approach to solving this problem, as it combines the use of fuzzy logic, which can handle imprecision and uncertainty in data, with adaptive learning, which allows the system to learn from the data and improve its performance over time.

The fuzzy adaptive learning control network (FALCN) and the Gaussian-functioned radial basis neural network (RBNN) are two deep learning segmentation models that are used in this paper's clustering-based segmentation method. Following image segmentation, the pertinent traits are gathered and fed into a radial basis neural network classifier. The proposed fuzzy system, unsupervised fuzzy neural networks, is efficient at classifying photos and can extract characteristics from raw images. FALCN was used to cluster the images. When a conventional fuzzy network system is subjected to noisy input, output neurons increase unnecessarily. Finally, random convolutional weights are employed to extract features from unlabeled data. Based on the outcomes of simulations, the suggested FALCN and RBNN classifier increased mean squared error values and accuracy for the JAFE, ORL, and UMIT datasets. The most significant contributions of FALCN-RBNN are the following:

- The FALCN-RBNN, which is crucial for enhancing the performance of the CBIR system, has a robust noise characteristic by identifying the indeterminate bit inside the visual input.
- FALCN-RBNN calculates the pixel value and difference before being multiplied by a fixed amount. Brightness changes are countered by this, strengthening one's ability to discriminate.
- To boost gradient amplitude, FALCN-RBNN filters out noise and looks for edges.

The article is arranged as follows: While Section 2 outlines prior work, Section 3 offers a strategy. The investigation is finished in Section 5, and Section 4 presents the experiment results.

2. Literature survey

Sudha and Ali [18] studied the evolution of image retrieval methods for distant sensing. These methods must be improved to find similar satellite images from massive databases. Retrieval tactics require successful feature extraction techniques. Identifying, collecting and showing key satellite picture characteristics have become increasingly difficult. The properties obtained determine the performance of image retrieval systems. Choosing the similarity measure and retrieval algorithms is essential to enhance the retrieval system.

Sanu and Tamase [19] recommended using a content-based image retrieval technique to avoid data loss and recover crucial information from photos. They suggested that this was the best method to achieve these objectives. Unsupervised J-seg segments images to decrease distortion. Using a probabilistic picture classification technique, a Bayesian classifier can give a region-based comparison. Each region's picture database has 20 satellite image features. A Bayesian classifier separates the query image's parts from other images in the database.

Padmashree Desai et al. [20] focused on retrieving archaeological monument images for the first time. Those who are interested in art and researchers in this field should thank this work for laying the foundation. With the help of morphological operators and a grey-level co-occurrence matrix (GLCM), this research proposed a 90% accurate automatic organization of monument pictures. Other investigations used techniques such as machine learning algorithms and various feature combination models.

Chandraprakash and Narayana [21] developed a CBIPR system that uses form features to retrieve satellite cloud pictures. They forecasted precipitation using meteorological satellite imagery to understand historical and contemporary climate systems better. MOSDAC, or the Archives of Meteorological and Oceanographic Satellite Data, was utilized for this investigation. Ocean Sat, Megha Tropiques, SARAL, KALPANA-1, INSAT and MOSDAC archives made MOSDAC archives possible. The mobile weather services offered by MOSDAC include notifications.

An alternative technique for image retrieval founded on the two most widely used methods, K-means and hierarchical clustering, was proposed by P. Pattanasethanon and B. Attachoo [22]. This study focused on CBIR, where the results were composed of various instances of unrelated feedback. Precision and recall levels were reported as the findings of the experimental investigation and were 70% and 50%, respectively.

Spatial information was added to the BoVW model's inverted index by Zafar et al. [23], and a brand-new approach to encoding images was given. The computation of visual words' universal matching spatial inclination links spatial information. This ensures data consistency independent of the orientation of the device. Geometrically similar comments are related. Each visual word triplet is assigned. The dimensions of orthogonal vectors influence the location of visible linear words in the histogram. Four datasets are used to evaluate the strategy.

The approach by Hor et al. [24] returns images by integrating local texture data from two separate texture descriptors. The entering image's color channels were first split. Two descriptors assessed local binary patterns, and preset pattern units were used to get texture information. Following feature extraction, distance-based similarity matching is conducted. The Simplicity database was used as a benchmark for the proposed technique's accuracy (91%), recall (90.3%) and efficiency (90.3%). Data analysis exposed that the projected technique had better accuracy than several well-known techniques.

Bani et al. [25] provided evidence that image recovery techniques include those that recover an image's contents based on texture, color, and geometry. The suggested method for image retrieval collects information on color, texture and texture locality in two spatial and frequency domains. This way, the image is filtered with a Gaussian filter, co-occurrence matrices are built in various directions, and statistical data are collected. This stage's goal is to extract locally noise-resistant textures. Next, a quantized histogram is created to collect spatial-domain color data globally.

The local vector to be used as the featured vector may be extracted using Dawood et al.'s [26] accessible, innovative CBIR method founded on color and texture cues. The texture is removed using Gabor wavelets, discrete wavelet transform and color moments. Directory descriptors are applied to

the feature vector to enhance its color and edge. This method offers good precision and recall when compared to earlier CBIR algorithms.

In Mistry et al. [27], color and texture topographies are merged to get the best possible retrieval presentation. This is so that a retrieval performance can be obtained efficiently, with no single attribute being more resilient than another. Because of this, the color moment is utilized for color extraction. Using the Gabor descriptor, textural qualities are retrieved. The properties are transmitted via color and edge directivity descriptor (CEDD).

Duan et al. [28] focused on face recognition. Face recognition systems have improved in the last 20 years. There are two main techniques for face recognition: extracting discriminative features from the beginning and designing effective classifiers to recognize various people. Local picture features outlive global ones and are more resistant to change. Most fields require prior knowledge. For face remodeling, the contextualized data suggests CA-LBFL. It contrasts with an existing feature-learning model.

An innovative content-based retrieval method that protects privacy was also developed by Ferreira et al. [29]. Additionally, their system protects color information using deterministic encryption techniques, enabling image retrieval without compromising privacy. They also permit the encryption of texturing data using probabilistic encryption techniques for further protection.

According to Kumar et al. [30], one of several distance measures can be used to extract and compare local properties. They simulated retrieval founded on regional picture topographies using five of the most used distance measurements to determine the most effective approach. Based on experimental results using a publicly available dataset of 9908 JPEG photos to evaluate their efficacy in discovering relevant images, the Manhattan L1 distance metric was shown to be the most exact and practical.

Uma Maheswaran et al. [31] effectively recovering explicit photos from a more extensive database is practically required for CBIR. They developed a special method that boosts CBIR precision by combining the Multi Texton Histogram and Micro Structure Descriptor. The suggested CBIR technique is based on a variety of visual elements, structure, and knowledge of how higher-level visual significant transfer and representation take place.

An approach for the multiscale local binary pattern (LBP) CBIR was provided by Srivatsava et al. in [32]. At different scales, the local binary pattern is generated utilizing combinations of eight neighbor pixels rather than a line of neighbors. The GLCM, a statistical technique, is used to create the final feature vector. The advantage of the proposed multiscale LBP method is that it overcomes single-scale LBP's drawbacks and provides a more reliable feature descriptor. It fixes some of the issues with earlier multiscale LBP algorithms and captures discernible large-scale elements of complex textures in a way that single-scale LBP cannot. The effectiveness of the proposed approach was assessed using the benchmark datasets Corel-1K, Corel-5K, Corel-10K, Olivia-2688 and GHIM-10K.

As a potent technique for enhancing CBIR performance, Yousuf et al. [33] introduced visual word fusion of the Scale Invariant Feature Transform (SIFT) and the Local Intensity Order Pattern (LIOP) descriptors. The performance review's findings have been verified. The four triangular components of a picture were used by Mehmood et al. [34] to construct weighted soft codebooks, triangular histograms and LIOP features. Each of the aforementioned methods for doing CBIR research had its drawbacks. For instance, past research techniques should have noticed ideas that had noise. Modern CBIR research methodologies also require more sophisticated computational methods. The suggested research plan will address these problems.

The primary focus of Lujia Lei et al.'s [35] research was the anti-noise performance of photo segmentation. Since using a kernel function prevents the application of Euclidean distance to kernel space, this work proposed a dual-neighborhood information limited deep fuzzy clustering based on kernel function (KDFKMS), which builds on prior work in the field of deep kernel-based fuzzy clustering (DFKM). Also, the neighborhood median and mean information of the current pixels were combined, and Euclidean distance was extended to kernel space.

Li Guo et al. [36] proposed, as a first step, building a new affinity matrix to store and show the image's spatial information as a predecessor. This was to help membership-regularized fuzzy clustering methods get good results when used for segmentation. In order to do this, the affinity value was determined by putting together information about pixels and regions, showing how two points in an image are related in a subtle way. Also, to decrease the effect of image noise, they used fixed cluster centers in the iteration of the algorithm. This means that the only thing that guides the updating of membership values is the prior information fused.

Table 1. Existing methods for image clustering and content-based image recovery on a noisy dataset.

Author	Techniques	Classes/Images	Dataset	Presentations
Nazir et al. [37]	Histogram examples include the edge histogram descriptor, the HSV color space histogram, and discrete wavelet treatments.	One thousand pictures are divided into ten categories.	Corel 1-K	retrieval of images based on content
Liu et al. [38]	Fusion of color histogram and LBP-based features	Vistex contains 640–864 pixel picture textures. The Brodatz and Vistex categories each include 16 images.	Brodatz, Vistex	Texture-based images retrieval
Duan et al. [28]	Acquisition of local binary features with context awareness	-	LFW, YTF, FERET	Faces' identification
Ahmed et al. [39]	Image features information fusion.	Groupings into ten distinct categories. In each category, there are 100 images	Corel 1000	Content-based image retrieval
Dawood et al. [26]	Multimedia information for locating photos based on different criteria.	Ten categories are present. There are 100 different-sized photos in each category.	Corel 1000	retrieval of images based on content

3. Proposed system

Depending on several parameters, retrieving artificial and natural background areas in image processing can be categorized as picture segmentation. Finding specific visual components requires this categorization. The provided image's formula (1) is represented by the supplied image F (p,q).

$$F(p,q) = NB(p,q) + \sum_{x=1}^{n} MM(p,q) + NO(p,q). \qquad (1)$$

Natural Background NB (p,q), Man-Made Things MM (p,q) and Noise NO (p,q) are the three categories. The images provide information on the surroundings, including natural and manufactured backdrops. The proposed framework is depicted in Figure 1. The number of clusters of two in the proposed system is fixed. Both natural and manufactured elements may be seen in this landscape.

Within groups, background pixel values were thought to follow Gaussian distributions that varied from cluster to cluster. It was believed that produced goods' values significantly deviated from the cluster distribution. The attributes of the natural setting and the manufactured objects are listed in the following table.
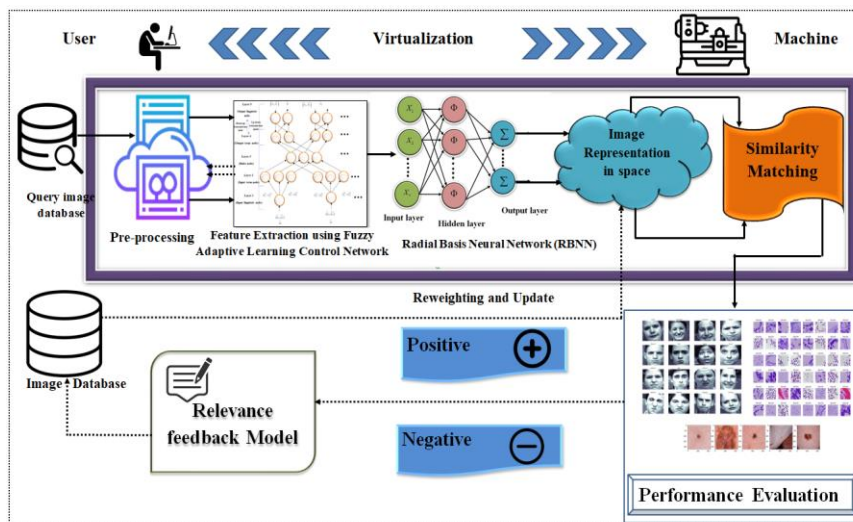

Figure 1. Proposed method of FALCN-RBNN.

3.1. Pre-processing

The two-color models that most closely approximate how people see color are HSV and CIELAB, and pre-processing considers these crucial visual characteristics. The block size and image quality are tightly related, regardless of the method. In terms of correlation, smaller blocks are preferable. Still, if they are too tiny, removing many coefficients from each part will be challenging without significantly changing the outcomes, particularly if the block has more volatility and data. We could construct the color map with less space if we quantized each color channel equally (as in the HSV color model). Fifty-four color combinations are produced using six bins for hue (360 alienated into six varieties of 60 each) and three compartments for saturation (purity divided into three fields of grayness). There are six hue bins (corresponding to the 360 degrees in the color space, divided into six ranges of 60 degrees each) and three value bins (corresponding to the brightness levels of black, intermediate and white). Image pre-processing is finished to remove noise and provide a high-quality image for feature extraction. Utilizing the Otsu threshold and Gaussian filtering, the objects in this suggested study are recognized. The technique offers details on the pixels in the foreground and background. Therefore, pixels with values of "1" signify objects, whereas those with values of "0" signify the background. Mathematics, smoothing operators and noise probability distributions are just a few academic areas where the Gaussian function is employed.

$$G(r,c) = \frac{1}{\sqrt{2\pi\sigma^2}} exp\left(-\frac{r^2+c^2}{2\sigma^2}\right). \tag{2}$$

This integral is 1 if and only if $\frac{1}{\sigma\sqrt{2\pi}}$ where, the Gaussian is the probability density function of

a generally distributed random variable with the expected value c = b and variance σ2 = c2. The equation above represents a picture as a Gaussian-functioned integer matrix. G in the equation stands for this function (r, c). The value of each integer indicates a pixel's exposure to light. The value of σ is used to denote the distribution's standard deviation. The weight greatly influences the coefficients of the Gaussian kernel. The coefficients along the mask's edge should be close to "0" [40].

3.2. Feature based matching and retrieval

Each database image is assessed using the designated distance metric and color space bins before being archived in a feature database. Each file contained in the collection is identified by name in the first column of the database, and each record includes a quantitative description of a copy's attributes. The contribution query image goes through the same process, but instead of having its features saved in a database, they are used as a point of comparison when comparing each entry in the database. After the comparison, a record is assigned a relevance assessment ranging from 0 to 1. The relevance value is used when sorting is required before results are output to the user. According to an ordered list of relevance scores, the images are displayed from most relevant to least relevant. The relevancy grade increases with the comparison between the query image and an image in the database.

3.3. Fuzzy adaptive learning control network (FALCN) clustering

Building a fuzzy rule foundation involves all layer-3 nodes working together. An engine for connectionist inference is provided by layers three and four. There is optional connectivity between the word node of a language and each rule node. This is true for the base layer (layer 3) and the next layer (layer 4) of connectivity. All language and term node linkages are present in layers 2 and 5. The arrows point toward typical signal flow whenever the network is in the process (later, it has been built and accomplished). Transmission of a signal will be indicated by an arrow moving in the direction of the transmission.

FALCN uses complement coding to normalize input-output training vectors. An n-dimensional $\mathbb{R}^n = nu = (u_1 u_2, \dots . u_n)$ vector is transformed into its [0; 1] complement, a 2n-dimensional n-dimensional vector, through normalization. Scaling is more uniform with complement coding.

$$u^{'} = (\overline{u}_1, \overline{u}_1^c, \overline{u}_2, \overline{u}_2^c, \dots , \overline{u}_n, \overline{u}_n^c) = (\overline{u}_1, 1 - \overline{u}_1, \overline{u}_2, 1 - \overline{u}_2 \dots , \overline{u}_n, \overline{u}_n), \qquad (3)$$

where $(\overline{u}_1, , \overline{u}_2, , \dots , \overline{u}_n) = \overline{u} = u/||u||$. Complement coding, as mentioned, aids in avoiding the problem of category proliferation. Categories are propagated via clustering based on fuzzy FALCN. To achieve the resonance condition for fuzzy clustering (11)-(13), future non-complement coding contributions must add more heaviness vectors to the origin or select different nodes. This can be prevented by using complement coding in input data pre-processing. Training vectors that normalize while maintaining amplitude are known as complement coding. Both desired output vectors and input state vectors are training vectors. Before being utilized for training, complement is coded during the FALCN pre-processing stage. There are weighted fan-in and fan-out connections between nodes in a typical neural network. An integration function (f) uses input from other nodes as proof or activation in calculating a node's net input [41].

$$ney - input = f\left(z_1^{(k)}, z_2^{(k)}, \ldots, z_p^{(k)}; w_1^{(k)}, w_2^{(k)}, \ldots w_p^{(k)}\right) \qquad (4)$$

where $z_i^{(k)}$ is the ith input to a node in layer k, and $w_i^{(k)}$ is the associated link's weight. The superscript indicates the layer number in the preceding calculation. This notation will also be used in the calculations that follow. Based on its net input, each node also generates a stimulation assessment.
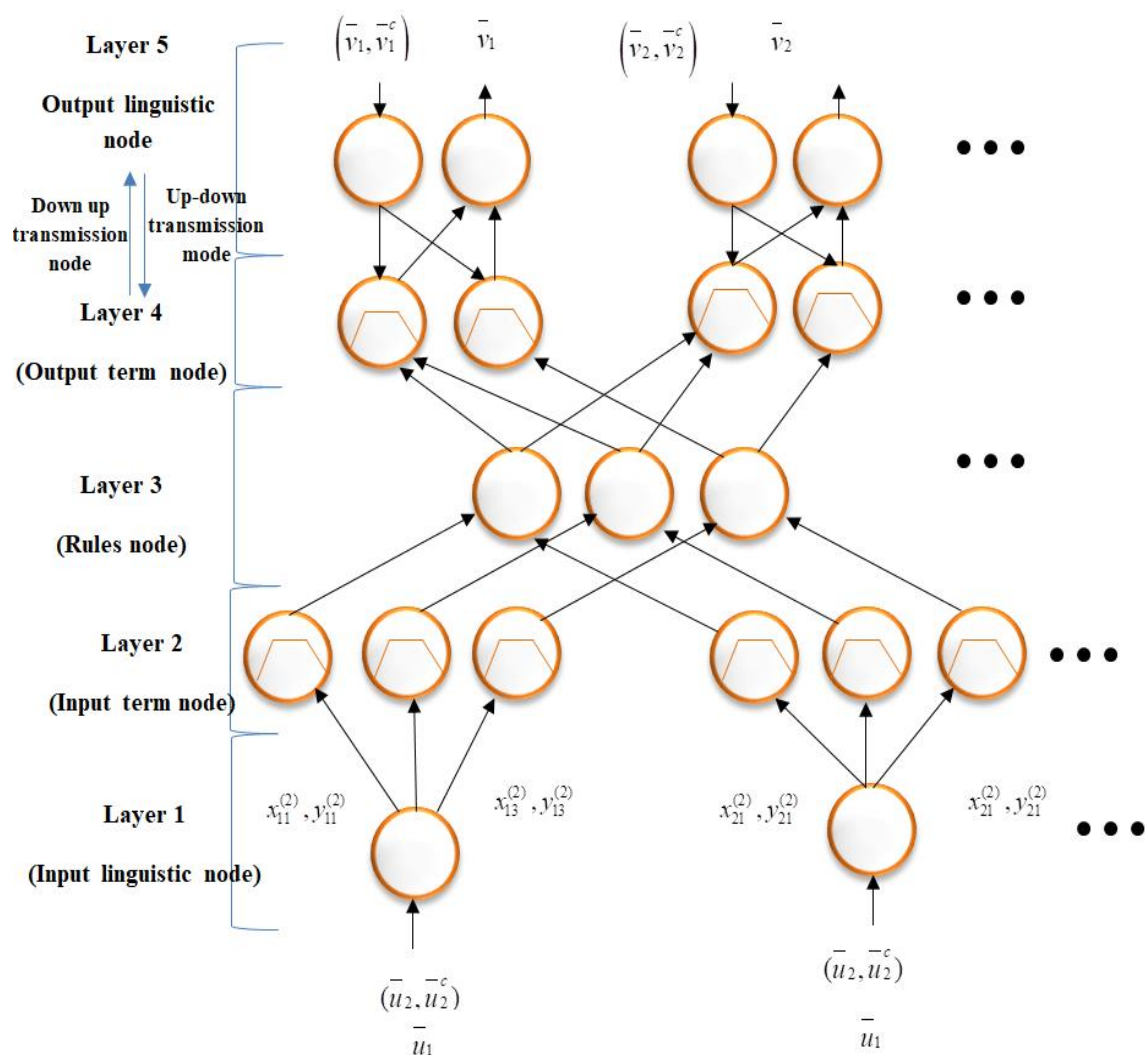
$$output = a(f(\cdot)). \qquad (5)$$

Figure 2. Fuzzy adaptive learning control network (FALCN).

The activation function is denoted by $a(\cdot)$. The following section will define the roles of the nodes in each of FALCN's five layers. Assume that the output space has m dimensions, whereas the input space has n.

The first layer consists of linguistic input nodes, corresponding to a different language input variable for each. Incoming signals are only relayed to higher layers by layer one nodes. As a result,

$f(\overline{u}_i, \overline{u}_i^c) = (\overline{u}_i, \overline{u}_i^c) = (\overline{u}_i, 1 - \overline{u})$, and

$$a(f(\cdot)) = f(\cdot). \tag{6}$$

Weight of the layer 1 link $w_i^{(1)}$ is given by the above equation. After complement coding, there are two outputs for each input node I, $\overline{u}_i^c$ and $1 - \overline{u}_i$.

For a linguistic variable in the input, input term nodes serve based on affiliation with a single dimension. Using a trapezoidal membership function,

$$f\left(z_{ij}^{(2)}\right) = \left[1 - g\left(z_{ij}^{(2)} - y_{ij}^{(2)}, \gamma_{ij}\right) - g\left(x_{ij}^{(2)} - z_{ij}^{(2)}, \gamma_{ij}\right)\right], \tag{7}$$

and $a(f(\cdot)) = f(\cdot),$

where $x_{ij}^{(2)}$ and $y_{ij}^{(2)}$ are their respective positions on the jth contribution period nodes and the ith contribution linguistic nodes' in trapezoidal membership function (see Figure 2). $z_{ij}^{(2)}ij$ denotes input from the ith input linguistic node (i.e., z (2) $ij = u_i$).

$$g(s, \gamma_{ij}) = \begin{cases} 1 \ if \ s\gamma_{ij} > 1, \\ s\gamma_{ij} \ if \ 0 \leq s\gamma_{ij} \leq 1, \\ 0 \ if \ s\gamma_{ij} < 0. \end{cases} \tag{8}$$

γ_{ij} controls how fuzzy the trapezoidal membership function is. γ_{ij} values below one denotes fuzzier, less distinct sets, while values over one denote separate groups. The outputs of n input term nodes are combined. This produces an n-dimensional membership function in the input space, with a single-term node for each dimension. Each linguistic contribution node contains the exact amount of word nodes. The number of sentences in each FALCN input variable is the same. Also affected are the linguistic nodes in the output. Linkages at layer two join linguistic input nodes to term nodes. Layer-2 links are capable of supporting two weights. The connections between input node I (which corresponds to x_i) and its jth term node are weighted, and $x_{ij}^{(2)}$ and $y_{ij}^{(2)}$ reflect those relationships (see Figure 2). In the equation, the two weights stand in for the membership function (5). There are $x_{ij}^{(2)}$ and $y_{ij}^{(2)}$ weights assigned to the input linguistic nodes $\overline{u}_i$ and $\overline{u}_i^c$ from node I. The FALCN clustering procedure in the initial learning phase will use $\overline{u}_i$ and $\overline{u}_i^c$ to identify $x_{ij}^{(2)}$ and $y_{ij}^{(2)}$. All other stages of FALCN's learning and daily operation only employ forward-thinking methods ($z_{ij}^{(2)} = \overline{u}_i$ in Eq (5)).

This layer's rule nodes represent fuzzy logic rules. The third layer, every layer of three nodes, has n input term nodes. In FALCN, the total number of input words and rule nodes is identical. The exact amount of terms are available for input for each FALCN is customizable. Layer 3 linkages fulfill the requirements of fuzzy logic. As a result, rule nodes carry out production activities.

$$f\left(z_i^{(3)}\right) = \prod_{i=1}^{n} z_i^{(3)} \text{ and } a(f(\cdot)) = f(\cdot). \tag{9}$$

A layer 3 node's $z_j^{(3)}$ input is its ith input, and the product is its inputs. In Layer 3, there is a single connection weight $w_j^{(3)}$. An n-dimensional membership function is created by using the production method from the previous equation, that is, the sum of the trapezoids in (5) over the i-th dimension. The multidimensional trapezoidal membership function is a membership function for a hyper box. The membership function on an input hyperbox is specified. The Layer-2 weights $x_{ij}^{(2)}$ and $y_{ij}^{(2)}$ determine the hyperbox corners regardless of i. $x_{ij}^{(2)}$ and $y_{ij}^{(2)}$ form the hyperbox's boundary in the ith dimension. A hyperbox is represented by the weight vector $\left[\left(x_{1j}^{(2)}, y_{1j}^{(2)}\right), \ldots, \left(x_{ij}^{(2)}, y_{ij}^{(2)}\right), \ldots, \left(x_{nj}^{(2)}, y_{nj}^{(2)}\right)\right]$ in the input space. Figure 2 shows a 2-D hyper box membership function (b). The fourth layer's m sets of output term nodes are connected to the rule nodes' output. This collection of output term nodes in the output space describes an m-dimensional trapezoidal (hyper box) membership function. The genetic algorithm (GA) will choose the layer three and layer four link types.

For Layer 4 output period nodes, two transmission modes are available: down-up and up-down (see Figure 2). Layer 4 links on red (active) rule nodes perform fuzzy OR in the down-up method, which yields the same outcome.

$$f\left(z_i^{(4)}\right) = max(z_1^{(4)}, z_2^{(4)}, \ldots, z_p^{(4)}) \text{ and} \tag{10}$$

$$a(f(\cdot)) = f(\cdot),$$

where $z_i^{(4)}$ stands for layer 4 i^{th} input, and period for the layer 3 rule node inputs. W is the link's weight, $w_{ij}^{(4)} = 1$. The nodes of layer five and this layer's up-down links are the nodes in up-down transmission mode, just like layer two. Each node represents one phrase from an output linguistic variable. Each linguistic output node has its output period node, resulting in an m-dimensional hyper box (association function) in the output space. The Layer 5 up-down transmission lines are given $x_{ij}^{(5)}$ and $y_{ij}^{(5)}$ weights. Output weights determine hyperbox. In the weight vector $\left[\left(x_{1j}^{(5)}, y_{1j}^{(5)}\right), \ldots, \left(x_{ij}^{(5)}, y_{ij}^{(5)}\right), \ldots, \left(x_{mj}^{(5)}, y_{mj}^{(5)}\right)\right]$, a hyperbox may be seen in the production space.

Layer 5: Each linguistic output node corresponds to a single output linguistic variable in this layer. Layer 5 has two types of nodes. The first type of node, like input language nodes, accomplishes up-down communication for training information (preferred productions) to feed into the network. There is such a node.

$$f\left(\overline{v}_i, \overline{v}_i^c\right) = \left(\overline{v}_i, \overline{v}_i^c\right) = \left(\overline{v}_i, 1\overline{v}_i\right) \text{ and} \tag{11}$$

$$a(f(\cdot)) = f(\cdot).$$

The normalized i^{th} component of the output vector is denoted by $\overline{v}_i$. Recall that output vectors are complement-coded as well. As a result, layer five transmission connections have two weights for each up-down link. Considering $x_{ij}^{(5)}$ and $y_{ij}^{(5)}$ in Figure 2, weights represent hyperbolas and their membership functions in the output space. Decision signals are sent downward by the second kind of node. Defuzzers need Layer-5 down-to-up transmission links to bind these nodes together. The center of area defuzzification method can be duplicated using the following functions.

$$f\left(z_i^{(4)}\right) = \sum_j w_{ij}^{(5)} z_j^{(5)} = \sum_j m_{ij}^{(5)} z_j^{(5)} \text{ and} \tag{12}$$

$$a(f(\cdot)) = \frac{f(\cdot)}{\sum_j z_j^{(5)}},$$

where $m_{ij}^{(5)} = \left(x_{ij}^{(5)} + y_{ij}^{(5)}\right)/2$ is the value at the center of the output membership function, and $z_j^{(5)}$ is the input of the jth period node to the ith output linguistic node. The absolute membership value is lowest in the fuzzy area's center. The membership value of other regions is 1. $w_{ij}^{(5)} = m_{ij}^{(5)} = \left(x_{ij}^{(5)} + y_{ij}^{(5)}\right)/2$, where $x_{ij}^{(5)}, y_{ij}^{(5)}$ are the weights of the five top-down layers.

The FALCN-RBNN learning approach for selecting the hyper box $(x_{ij}\text{'s and } y_{ij}\text{'s})$ the construction will look like its predecessor. It will also comprehend fuzzy logic links and rules at the third and fourth layers, including the precondition and following linkages of rule nodes.

3.4. Radial basis function

Because of their fundamental design, radial basis neural networks can be put to use in many different contexts. By employing the cuckoo search technique, the radial basis network model is improved. RBF Gaussian curve is given by the equation in the next section. The RBF evaluates network performance using several harmonic and polynomial expressions. This is how the polyharmonic function is expressed:

$$R(b) = e^{-kr^2}, \tag{13}$$

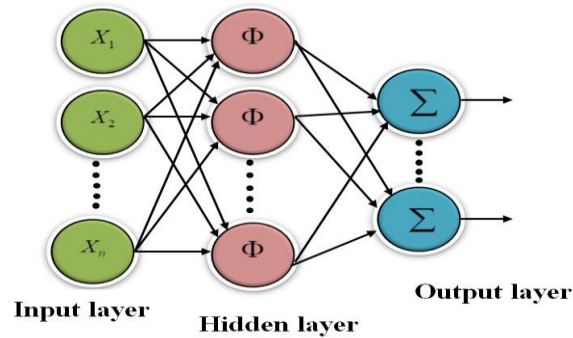where

$$r = ||b - d_n||. \tag{14}$$

Figure 3. Simulate block diagram of RBNN.

The equation above can be written as:

$$r = \sqrt{(b - d_n)^T (b - d_n)}. \tag{15}$$

Use this function to represent Gaussian and polyharmonic functions roughly. To find the MSE in this case, a cuckoo search strategy is used to optimize the feature. The mean square error is determined as follows:

$$MSE = \frac{1}{N} \sum_{n}^{N} (input_n - reconstructed_n)^2. \tag{16}$$

The input and reconstructed pictures' doubling functions are added up and subtracted to determine MSE. The radial basis for the part of the absolute value is written as follows:

$$\phi(b) = \phi(||b||). \tag{17}$$

Because the dimensionality has changed, the next position is the location in the radial basis function that comes after the origin. The variable dimension is denoted by the letter d, which is written as

$$\phi(b, d) = \phi(||b - d_n||). \tag{18}$$

RBF employs the Euclidean distance defined in (19).

$$B(n) = \sum_{n=1}^{N} w_n \varphi(||b - d||). \tag{19}$$

Using a cuckoo search algorithm, the non-linear function is optimized. The two-fold cross-validation technique's feature extraction phase involves training the hidden nodes [39].

4. Results and discussion

4.1. Experimental configuration

Here, the consequences of the experiment and associated debates are presented. Let us start with

the tools we will be using for the investigation. Listed below are the datasets, measurements and parameters. The second part of our report includes experimental results for FALCN-RBNN and other algorithms. Next, execute FALCN-RBNN and different algorithms on noisy datasets. Our section shows how performance can change depending on a few key variables. A study is done on how fuzzy membership functions affect FALCN-RBNN.

The average of each statistic was obtained after each experiment had been run 100 times. MATLAB 2021a is run on a computer equipped with 64 GB of RAM and an Intel Xenon CPU E5-2680 v3 @ 2.50 GHz to perform all other algorithms.

This image retrieval method employs a test dataset. There are 9908 photos in the collection as a whole. The entire collection consists of full-color images. We use the popular 10k dataset from Stanford, which includes a variety of objects and settings like landscapes, flowers, flags, animals, etc. Every image in the collection is in JPEG format and has a resolution of 128 × 96. The dataset is accessible online at wangz/image.vary.jpg.tar at infolab.stanford.edu.

The number of photos in each dataset category may vary between various datasets. As a result, depending on the datasets used, the algorithm's performance may change. An average is created to determine how well it worked using the results from the retrieval and accuracy. Here, the dataset may be positioned as the user sees fit. Only evaluation and demonstration purposes are served by using the sample dataset.

4.2. Performance analysis

The retrieval speed and accuracy metrics can be used to assess the presentation of any copy retrieval system. This methodology looks into the Rand index, Purity, Accuracy, Execution Time, RMSE, Training and Testing Validations, among other things. The collection of suitable photographs and the retrieval set will differ from what is shown. A group of pictures in the database correspond to the image you searched for. The relevance or irrelevance of ideas is deemed. In our clustering testing, three datasets are used. Table 2 lists each dataset's classes, attributes and input patterns.

Table 2. The datasets that we used in our tests are listed below.

Number	Dataset	No. of Classes	No. of attributes	No. of input pattern
1	ORL [30]	40	1024	400
2	UMIST [11]	20	1024	575
3	JAFFE [21]	10	1024	213

The NMI, RI and purity measures used in this study are used to assess the effectiveness of the clustering procedure. A standard metric for evaluating the caliber of clustering findings is the NMI derived from information theory and probability theory. The justification is as seen below:

$$NMI(y, y^{predict}) = \frac{I(y, y^{predict})}{\sqrt{H(y)H(y^{predict})}}. \tag{20}$$

$I(y, y^{predict})$ stands for the mutual information of y and $y^{predict}$, and $H(y)$ and $H(y^{predict})$ are for its entropy in Eq (20). Ground truth for the patterns is represented by $y^{predict}$, and clustering outcomes are represented by y and $y^{predict}$. Poor clustering results are penalized by "RI."

$$RI = \frac{TP+TN}{TP+FP+FN+TN}. \tag{21}$$

False positives, false negatives, and genuine negatives. These are the pairwise distributions of Rhode Island. FP denotes the number of ground truth partitions that do not include predicted point pairs. $TP + FP + FN + TN = \frac{N*(N-1)}{2}$. Purity is indicative of quality.

$$Purity = \frac{1}{N}\sum_{m \in M} \max_{d \in D} |m \cap d|. \tag{22}$$

m is one of a collection of clusters that make up m. It is a member of the class D. Since the presence of many clusters is not penalized by this metric, the purity value can be increased by amassing more data.

4.2.1. Normalized mutual information (NMI)

Table 3 and Figure 4 explain the normalized mutual information analysis of the FALCN-RBNN technique with other existing systems. The results demonstrate that the suggested strategy has the highest normalized mutual information compared to all other alternatives. The proposed method has a normalized mutual information of 0.753 when applied to the JAFE dataset, while it is 0.473, 0.583, 0.683 and 0.492 for UMFNN, FNN, K-means and LE, respectively. Similarly, with the ORL dataset, the proposed method has a normalized mutual information of 0.793, while it is 0.403, 0.553, 0.643 and 0.536 for UMFNN, FNN, K-means and LE, respectively. With the UMIT dataset, the proposed method has a normalized mutual information of 0.732, while it is 0.452, 0.504, 0.621 and 0.432 for UMFNN, FNN, K-means and LE, respectively.
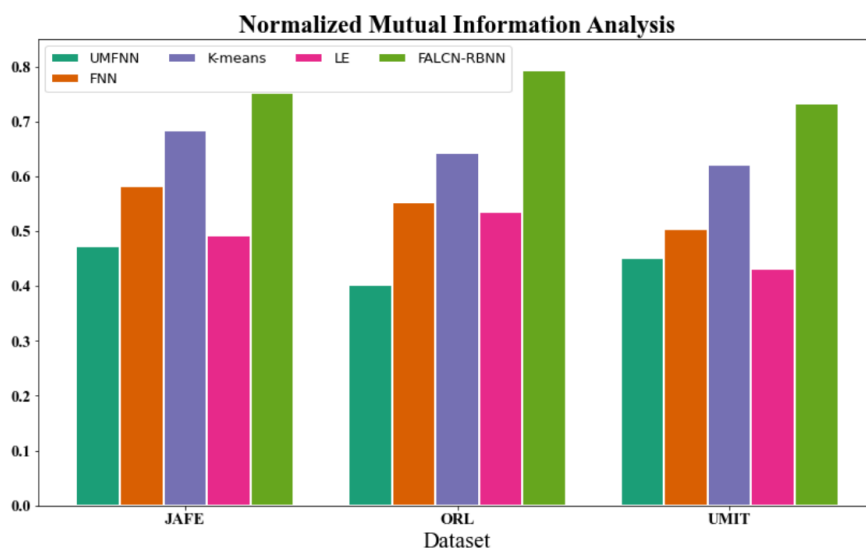

Figure 4. Normalized mutual information analysis for FALCN-RBNN method with existing systems.

**Table 3.** Normalized mutual information Analysis for FALCN-RBNN method with existing systems.

Dataset	UMFNN	FNN	K-means	LE
JAFE	0.473	0.583	0.683	0.492
ORL	0.403	0.553	0.643	0.536
UMIT	0.452	0.504	0.621	0.432

4.2.2. Rand index (RI)

Table 4 and Figure 5 explain the Rand index investigation of the FALCN-RBNN technique with other existing approaches. The projected approach has a Rand index of 0.983, whereas it is 0.843, 0.753, 0.893 and 0.863 for UMFNN, FNN, K-means and LE, respectively, with the JAFE dataset. Similarly, with the ORL dataset, the proposed method has a Rand index of 0.932, while it is 0.942, 0.782, 0.853 and 0.803 for UMFNN, FNN, K-means and LE, respectively. Similarly, with the UMIT dataset, the proposed method has a Rand index of 0.973, while it is 0.964, 0.732, 0.762 and 0.795 for UMFNN, FNN, K-means and LE, respectively.

Table 4. Rand index analysis for FALCN-RBNN method with existing systems.

Dataset	UMFNN	FNN	K-means	LE	FALCN-RBNN
JAFE	0.843	0.753	0.893	0.863	0.983
ORL	0.942	0.782	0.853	0.803	0.932
UMIT	0.964	0.732	0.762	0.795	0.973
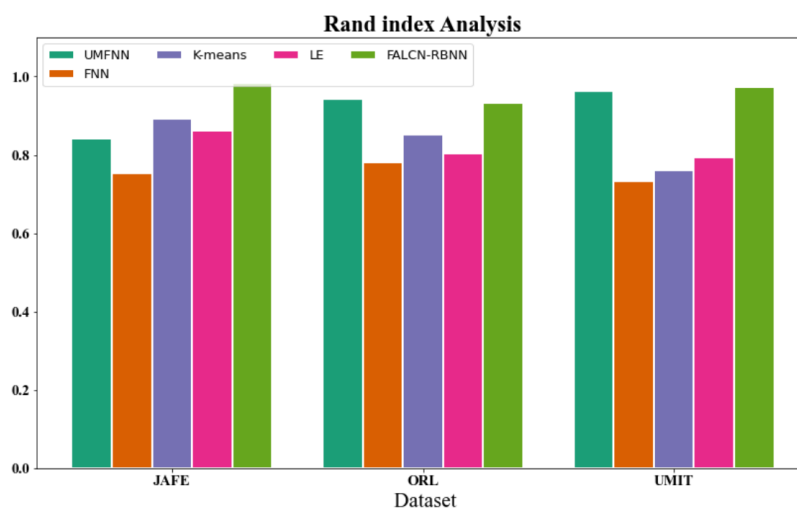
Figure 5. Rand index analysis for FALCN-RBNN method with existing systems.

4.2.3. Purity

Table 5 and Figure 6 explain the Purity analysis of the FALCN-RBNN technique with other existing techniques. The data demonstrate that the projected approach performs better with Purity associated with different styles in every aspect. The proposed method has a Purity of 0.973, whereas

it is 0.874, 0.903, 0.863 and 0.881 for UMFNN, FNN, K-means and LE, respectively. Similarly, with the ORL dataset, the proposed method has a Purity of 0.899, while it is 0.940, 0.962, 0.832 and 0.812 for UMFNN, FNN, K-means and LE, respectively. Similarly, with the UMIT dataset, the proposed method has a Purity of 0.993, while it is 0.952, 0.942, 0.922 and 0.803 for UMFNN, FNN, K-means and LE, respectively.

Table 5. Purity evaluation of the FALCN-RBNN method using existing systems.

Dataset	UMFNN	FNN	K-means	LE	FALCN-RBNN
JAFE	0.874	0.903	0.863	0.881	0.973
ORL	0.940	0.962	0.832	0.812	0.899
UMIT	0.952	0.942	0.922	0.803	0.993
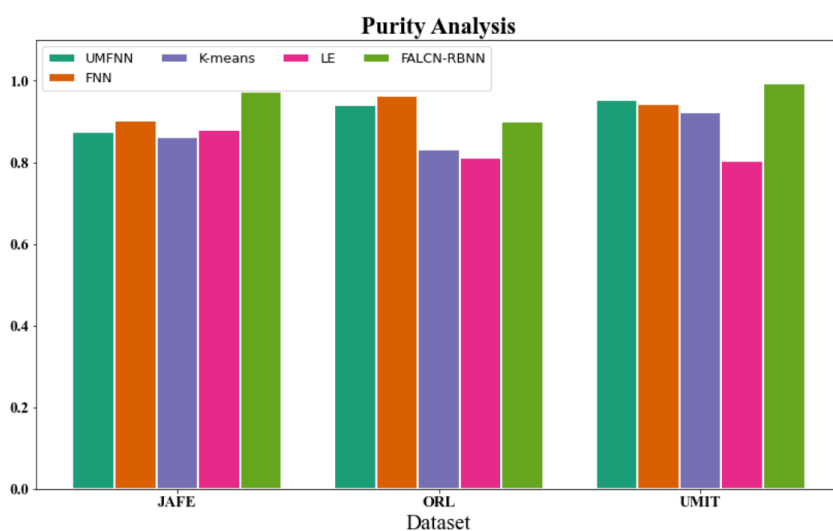
Figure 6. Purity nalysis for FALCN-RBNN method with existing systems.

4.2.4. Accuracy

In Figure 7 and Table 6, the accuracy of the FALCN-RBNN method is compared to those of other existing approaches. For instance, the UMFNN, FNN, K-means and LE models have accuracy values of 93.765%, 89.076%, 87.965% and 90.765%, while the FALCN-RBNN model, with 100 clusters, has an accuracy of 94.653%. On the other hand, the FALCN-RBNN model performed well with a range of data sizes. Similarly, the accuracy of FALCN-RBNN under 500 clusters is 96.547%, compared to accuracy values of 93.432%, 89.123%, 88.976% and 91.742% for UMFNN, FNN, K-means and LE models.

Table 6. Accuracy analysis for FALCN-RBNN technique with existing systems.

No of Clusters	UMFNN	FNN	K-means	LE	FALCN-RBNN
100	93.765	89.076	87.965	90.765	94.653
200	93.643	88.965	87.654	91.432	95.374
300	92.754	89.654	88.043	90.198	95.276
400	92.965	88.321	87.234	91.965	95.187
500	93.432	89.123	88.976	91.742	96.547
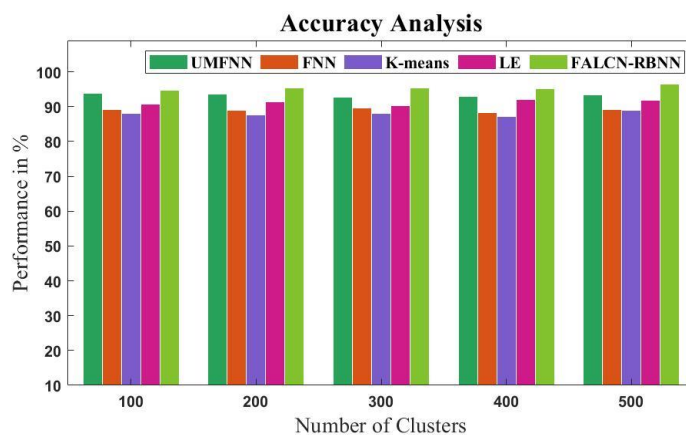
Figure 7. Accuracy analysis for FALCN-RBNN technique with existing systems.

4.2.5. Execution time

The comparison of the FALCN-RBNN technique's execution time analysis with existing designs is shown in Table 7 and Figure 8. The data demonstrates that the FALCN-RBNN procedure is better than the competing techniques. In contrast to other existing approaches like UMFNN, FNN, K-means and LE, which have execution times of 5.536 sec, 3.926 sec, 3.049 sec and 2.73 sec, respectively, FALCN-RBNN has taken only 1.029 sec to run with 100 clusters. Similarly, the FALCN-RBNN technique completes execution for 500 groups in 2.038 seconds, while the UMFNN, FNN, K-means and LE take 6.636 seconds and 5.43 4.928 seconds and 3.253 seconds, respectively.

Table 7. Analysis of FALCN-RBNN method execution time with existing systems.

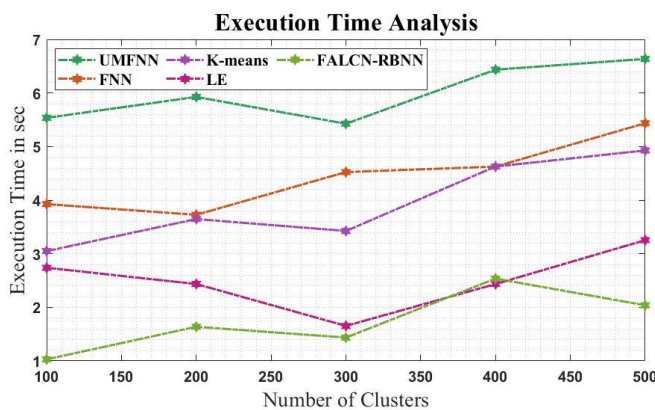| No of Clusters	UMFNN	FNN	K-means	LE	FALCN-RBNN
100	5.536	3.926	3.049	2.738	1.029
200	5.926	3.726	3.647	2.435	1.637
300	5.426	4.524	3.425	1.653	1.435
400	6.435	4.626	4.627	2.435	2.536
500	6.636	5.436	4.928	3.253	2.038

Figure 8. Analysis of FALCN-RBNN method execution time with existing systems.

4.2.6. RMSE

Figure 9 and Table 8 demonstrate a comparative RMSE examination of the FALCN-RBNN method with other existing approaches. The figure demonstrations that the deep learning method has resulted in higher performance with a lower RMSE value. For sample, with 100 clusters, the RMSE value is 35.837% for FALCN-RBNN, whereas the UMFNN, FNN, K-means and LE models have got slightly higher RMSE values of 45.847%, 40.827%, 38.324% and 37.02%, respectively. On the other hand, the FALCN-RBNN model has demonstrated maximum performance with low RMSE values across various data sizes. Similarly, FALCN-RBNN's RMSE value under 500 clusters is 36.028%, whereas the RMSE value is 46.243%, 44.837%, 41.826% and 38.947% for UMFNN, FNN, K-means, and LE models, respectively.

Table 8. RMSE analysis for FALCN-RBNN method with existing systems.

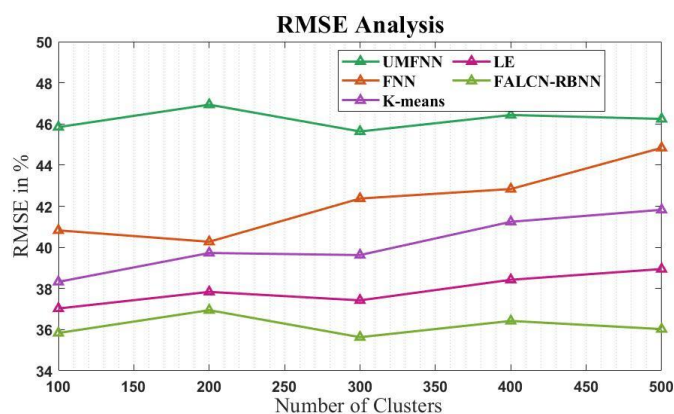| No of Clusters	UMFNN	FNN	K-means	LE	FALCN-RBNN
100	45.847	40.827	38.324	37.029	35.837
200	46.937	40.273	39.727	37.836	36.948
300	45.634	42.374	39.626	37.4245	35.634
400	46.435	42.836	41.243	38.425	36.425
500	46.243	44.837	41.826	38.947	36.028

Figure 9. RMSE analysis for FALCN-RBNN method with existing systems.

4.2.7. Peak signal noise-to-ratio (PSNR)

Figure 10 and Table 9 show a PSNR comparison of the FALCN-RBNN method with other known methodologies. The figure illustrates that the deep learning method has better PSNR presentation. For example, with 100 clusters, the PSNR value for FALCN-RBNN is 90.635%, whereas the UMFNN, FNN, K-means and LE models have PSNR values of 85.222%, 87.635%, 84.987% and 89.653%, correspondingly. The FALCN-RBNN model performed best with varying data sizes. Likewise, the PSNR value of FALCN-RBNN under the 500 clusters is 91.437%, whereas it is 87.937%, 88.837%, 85.635% and 89.5% for UMFNN, FNN, K-means and LE models, respectively.

Table 9. PSNR analysis for FALCNN-RBNN method with existing systems.

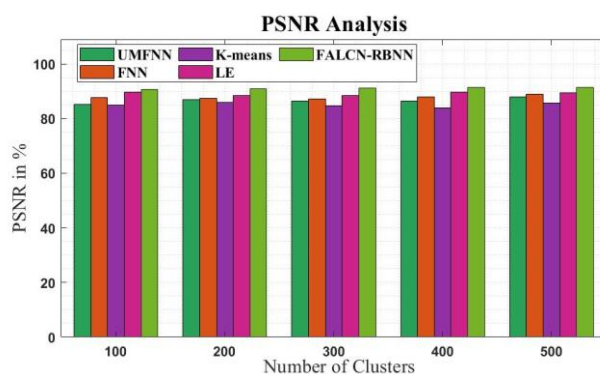| No of Clusters	UMFNN	FNN	K-means	LE	FALCN-RBNN
100	85.222	87.635	84.987	89.653	90.635
200	86.846	87.434	85.864	88.543	90.892
300	86.534	87.213	84.736	88.321	91.223
400	86.435	88.039	84.032	89.726	91.536
500	87.937	88.837	85.635	89.534	91.437

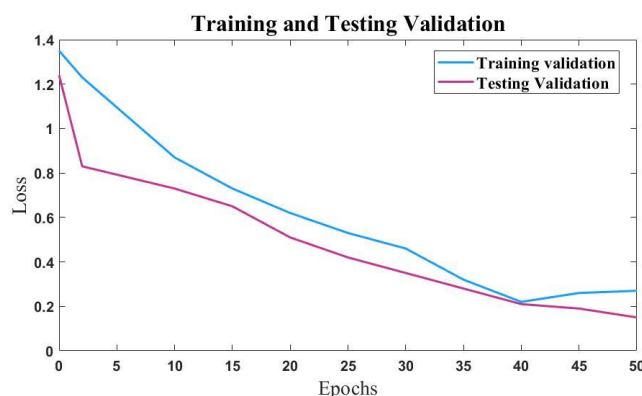**Figure 10.** PSNR Analysis for FALCNN-RBNN method with existing systems.

Figure 11. Training and testing validation analysis for FALCNN-RBNN method with existing systems.

4.2.8.   Training and testing validation

Table 10 and Figure 11 detail the training and testing validation analysis for the FALCN-RBNN approach using current platforms. The data showed that the proposed FALCN-RBNN approach did well in all respects. The FALCN-RBNN's training and testing validation are 0.87 and 0.73, with ten epochs. Similarly, under 50 generations, the FALCN-RBNN's training and testing validation coefficients are 0.27 and 0.15, respectively.

Table 10. Training and testing validation analysis for FALCNN-RBNN method with existing systems.

Epochs	Training validation	Testing validation
0	1.35	1.24
2	1.23	0.83
10	0.87	0.73
15	0.73	0.65
20	0.62	0.51
25	0.53	0.42
30	0.46	0.35
35	0.32	0.28
40	0.22	0.21
45	0.26	0.19
50	0.27	0.15

5.   Conclusions

This study utilized the Gaussian function, RBNN and FALCN to cluster the data using deep learning segmentation. For photo grouping, CBIR uses the improved FALCN network. The images are only evaluated on the same cluster rather than the entire database, considerably reducing retrieval time when using the suggested technique. We used the color, texture and shape feature vectors from photographs as network input elements. The dominant triple (HSV), which serves as a marker for the color information in the image, is used to build the quantized HSV joint histogram in the copy section. The edge angle histogram offers shape information, but entropy and the extreme entry of co-occurrence criteria provide texture information. Clustering based on color, texture and form generated reliable outcomes. The FALCN model's first inputs were susceptible to noise. An enhanced noise-resistant FALCN clustering method was then provided. The proposed technique alters nodes differently for committed and uncommitted nodes. Multiresolution gradient orientation improved texture identification by strengthening the link among texture, local contrast information and color. The performance will be enhanced by developing a clustering algorithm and a better method for extracting image information. CBIR requires the extraction of semantic information from photographs. They are utilizing current methods like K-means, Laplacian embedding (LE), unsupervised multilayer fuzzy neural network (UMFNN) and unsupervised multilayer fuzzy neural network (FNN). This study discovered that the models had little impact on prediction accuracy. The proposed model took first place with an overall accuracy of 96.547% in determining whether a user would fit into a particular category. Therefore, developing a local and global property-based picture retrieval system that respects

privacy will be the focus of future efforts. We want to create a decision-making process that keeps high precision while reducing the size of the codebook.

Use of AI tools declaration

Acknowledgments

Conflict of interest

There is no conflict of interest, according to the authors.

References

1. C. Zhang, CNN-VWII: An efficient approach for large-scale video retrieval by image queries, *Pattern Recogn. Lett.*, **123** (2019), 82–88. https://doi.org/10.1016/j.patrec.2019.03.015

2. A. Shinde, A. Rahulkar, C. Patil, Content based medical image retrieval based on new efficient local neighborhood wavelet feature descriptor, *Biomed. Eng. Lett.*, **9** (2019), 387–394. https://doi.org/10.1007/s13534-019-00112-0

3. P. Subbulakshmi, M. Prakash, Mitigating eavesdropping by using fuzzy based mdpop-q learning approach and multilevel Stackelberg game theoretic approach in wireless CRN, *Cogn. Syst. Res.*, **52** (2018), 853–861. https://doi.org/10.1016/j.cogsys.2018.09.021

4. M. Indu, K. V. Kavitha, Survey on sketch-based image retrieval methods, *International Conference on Circuit, Power, and Computing Technologies (ICCPCT)*, Nagercoil, India, 2016, 1–4. https://doi.org/10.1109/ICCPCT.2016.7530358

5. S. K. Panigrahi, S. Gupta, P. K. Sahu, Curvelet-based multiscale denoising using non-local means & guided image filter, *IET Image Process.*, **12** (2018), 909–918. https://doi.org/10.1049/iet-ipr.2017.0825

6. J. Xu, L. Yun, X. Zheng, Forensic detection of Gaussian low pass filtering in digital images, *Proceedings of the 8th International Congress on Image and Signal Processing (CISP)*, Shenyang, China, 2015, 819–823. https://doi.org/10.1109/CISP.2015.7407990

7. Y. F. Lu, Extended biologically inspired model for object recognition based on oriented Gaussian–Hermite moment, *Neurocomputing*, **139** (2014), 189–201. https://doi.org/10.1016/j.neucom.2014.02.046

8. S. Wang, J. Zhang, T. X. Han, Z. Miao, Z. Miao, Sketch-based image retrieval through hypothesis-driven object boundary selection with HLR descriptor, *IEEE T. Multimedia*, **7** (2015), 1045–1057. https://doi.org/10.1109/TMM.2015.2431492

9. R. Mandal, P. P. Roy, U. Pal, M. Blumenstein, Bag-of-visual-words for signature-based multi-script document retrieval, *Neural Comput. Appl.*, **31** (2019), 6223–6247. https://doi.org/10.1007/s00521-018-3444-y

10. H. Dawood, M. H. Alkinani, A. Raza, H. Dawood, R. Mehboob, S. Shabbir, Correlated microstructure descriptor for image retrieval, *IEEE Access*, **7** (2019), 55206–55228. https://doi.org/10.1109/ACCESS.2019.2911954

11. M. N. Sharath, T. M. Rajesh, M. Patil, Design of optimal metaheuristics based pixel selection with homomorphic encryption technique for video steganography, *Int. J. Inf. Tecnol*. **14** (2022), 2265–2274. https://doi.org/10.1007/s41870-022-01005-9

12. P. Mohan, M. Subramanian, V. A. Sambath, Gradient Boosted Decision Tree-Based Influencer Prediction in Social Network Analysis, *Big Data Cogn. Comput*. **7** (2023), 6. https://doi.org/10.3390/bdcc7010006

13. Z. Zhao, X. Li, B. Luan, W. Jiang, W. Gao, S. Neelakandan, Secure Internet of Things (IoT) using a Novel Brooks Iyengar Quantum Byzantine Agreement-centered lockchain Networking (BIQBA-BCN) Model in Smart Healthcare, *Inf. Sci.*, **629** (2023), 440–455. https://doi.org/10.1016/j.ins.2023.01.020

14. T. Veeramani, S. Bhatia, Fida Hussain Memon, Design of fuzzy logic-based energy management and traffic predictive model for cyber physical systems, *Comput. Electr. Eng.*, **102** (2022),108135, https://doi.org/10.1016/j.compeleceng.2022.108135.

15. I. Couso, C. Borgelt, E. Hüllermeier, Rudolf Kruse, Fuzzy sets in data analysis, From statistical foundations to machine learning, *IEEE Comput. Intell. Mag.*, **14** (2019), 31–44. https://doi.org/10.1109/MCI.2018.2881642

16. Q. Wang, X. Wang, C. Fang, W. Yang, Robust fuzzy c-means clustering algorithm with adaptive spatial & intensity constraint and membership linking for noise image segmentation, *Appl. Soft Comput.*, **92** (2020), 106318. https://doi.org/10.1016/j.asoc.2020.106318

17. S. Satpathy, M. Prakash, S. Debbarma, A. S. Sengupta, B. K. Bhattacaryya, Design a FPGA, fuzzy based, insolent method for prediction of multi-diseases in rural area, *J. Intell. Fuzzy Syst.*, **37** (2019), 7039–7046. https://doi.org/10.3233/JIFS-181577

18. N. Ali, B. Zafar, F. Riaz, A hybrid geometric spatial image representation for scene classification, *PLoS One*, **13** (2018), 203339. https://doi.org/10.1371/journal.pone.0203339

19. S. G. Sanu, P. S. Tamase, Satellite image mining using content-based image retrieval, *Int. J. Eng. Sci*, **14** (2017), 13928.

20. P. Desai, J. Pujari, N. H. Ayachit, Classification of Archaeological Monuments for Different Art forms with an Application to CBIR, *2013 International Conference on Advances in Computing, Communications and Informatics (ICACCI)*, Mysore, India, 2013, 1108–1112. https://doi.org/10.1109/ICACCI.2013.6637332

21. D. Chandraprakash, M. Narayana, Content based satellite cloud image retrieval and rainfall estimation using shape features, *SSRG-IJGGS*, **4** (2017), 34–39. https://doi.org/10.14445/23939206/IJGGS-V4I2P105

22. P. Pattanasethanon1, B. Attachoo, An alternative approach for unsupervised cluster-based image retrieval, *Int. J. Phy. Sci.*, **7** (2021), 5498–5510. https://doi.org/10.5897/IJPS11.1287

23. B. Zafar, R. Ashraf, N. Ali, M. Ahmed, S. Jabbar, S. A. Chatzichristofis, Image classification by addition of spatial information based on histograms of orthogonal vectors, *PLoS One*, **13** (2018), 0198175. https://doi.org/10.1371/journal.pone.0198175

24. N. Hor, F. E. Shervan, Image retrieval approach based on local texture information derived from predefined patterns and spatial domain information, 2019. https://doi.org/10.48550/arXiv.1912.12978

25. N. T. Bani, S. Fekri-Ershad, Content-based image retrieval based on combination of texture and colour information extracted in spatial and frequency domains, *Electron. Libr.*, **37** (2019), 650–666. https://doi.org/10.1108/EL-03-2019-0067

26. H. Dawood, M. H. Alkinani, A. Raza, H. Dawood, R. Mehboob, S. Shabbir, Correlated microstructure descriptor for image retrieval, *IEEE Access*, **7** (2019), 55206–55228. https://doi.org/10.1109/ACCESS.2019.2911954

27. Y. Mistry, D. Ingole, M. Ingole, Content based image retrieval using hybrid features and various distance metric, *J. Electr. Syst. Inf. Technol.*, **5** (2017), 878–888. https://doi.org/10.1016/j.jesit.2016.12.009

28. Y. Duan, J. Lu, J. Feng, J. Zhou, Context-aware local binary feature learning for face recognition, *IEEE T. Pattern Anal. Mach. Intell.*, **40** (2018), 1139–1153. https://doi.org/10.1109/TPAMI.2017.2710183

29. B. Ferreira, J. Rodrigues, J. Leitao, H. Domingos, Practical privacy-preserving content-based retrieval in cloud image repositories, *IEEE T. Cloud Comput.*, **7** (2017), 784–798. https://doi.org/10.1109/TCC.2017.2669999

30. V. A. Kumar, Coalesced global and local feature discrimination for content-based image retrieval, *Int. J. Inf. Technol.*, **9** (2017), 431–446. https://doi.org/10.1007/s41870-017-0042-7

31. V. Sambath, R. A. M. Ramanujam, M. Sammeta, Deep learning enabled cross-lingual search with metaheuristic web-based query optimization model for multi-document summarization, *Concurr. Comput. Pract. Exper.*, **35** (2022), e7476. https://doi.org/10.1002/cpe.7476

32. P. Srivastava, A. Khare, Utilizing multiscale local binary pattern for content-based image retrieval, *Multimed. Tools Appl.*, **77** (2018), 12377–12403. https://doi.org/10.1007/s11042-017-4894-4

33. M. Yousuf, Z. Mehmood, H. A. Habib, T. Mahmood, T. Saba, A. Rehman, et al., A novel technique based on visual words fusion analysis of sparse features for effective content-based image retrieval, *Math. Probl. Eng.*, **2018 (**2018), 2134395. https://doi.org/10.1155/2018/2134395

34. Z. Mehmood, N. Gul, M. Altaf, T. Mahmood, T. Saba, A. Rehman, et al., Scene search based on the adapted triangular regions and soft clustering to improve the effectiveness of the visual-bag-of-words model, *J. Image Video Proc.*, **2018** (2018), 48. https://doi.org/10.1186/s13640-018-0285-7

35. L. Lei, C. Wu, X. Tian, Robust deep kernel-based fuzzy clustering with spatial information for image segmentation, *Appl. Intell.*, **53** (2023), 23–48. https://doi.org/10.1007/s10489-022-03255-3

36. L. Guo, P. Shi, L. Chen, C. Chen, W. Ding, Pixel and region level information fusion in membership regularized fuzzy clustering for image segmentation, *Inform. Fusion*, **92** (2023), 479–497. https://doi.org/10.1016/j.inffus.2022.12.008

37. A. Nazir, R. Ashraf, T. Hamdani, N. Ali, Content based image retrieval system by using HSV color histogram, discrete wavelet transforms and edge histogram descriptor, *2018 International Conference on Computing, Mathematics and Engineering Technologies (iCoMET).*, Sukkur, Pakistan, 2018, 1–6. https://doi.org/10.1109/ICOMET.2018.8346343

38. P. Liu, J. M. Guo, K. Chamnongthai, H. Prasetyo, Fusion of color histogram and LBP-based features for texture image retrieval and classification, *Inf. Sci.*, **390** (2017), 95–111. https://doi.org/10.1016/j.ins.2017.01.025

39. K. T. Ahmed, M. A. Iqbal, A. Iqbal, Content based image retrieval using image features information fusion, *Inform. Fusion*, **51** (2018), 76–99. https://doi.org/10.1016/j.inffus.2018.11.004

40. N. Subramani, A. Mardani, P. Mohan, A. R. Mishra, P. Ezhumalai, A fuzzy logic and DEEC protocol-based clustering routing method for wireless sensor networks, *AIMS Mathematics*, **8** (2023), 8310–8331. https://doi.org/10.3934/math.2023419

41. C. J. Lin, C. T. Lin, An ART-based fuzzy adaptive learning control network, *IEEE T. Fuzzy Syst.*, **5** (1997), 477–496. https://doi.org/10.1109/91.649900